



# Composite of lead-free halide perovskite $\text{Cs}_3\text{Bi}_2\text{Br}_9$ with $\text{TiO}_2$ as an efficient photocatalyst for $\text{C}(\text{sp}^3)\text{--H}$ bond activation

Zihao Cui<sup>a,b,1</sup>, Qianqian Zhang<sup>a,1</sup>, Hui Fu<sup>a</sup>, Qihao Liu<sup>b</sup>, Xiaolei Liu<sup>a</sup>, Yaqiang Wu<sup>a</sup>, Peng Gao<sup>a</sup>, Zeyan Wang<sup>a</sup>, Zhaoke Zheng<sup>a</sup>, Hefeng Cheng<sup>a</sup>, Yuanyuan Liu<sup>a</sup>, Ying Dai<sup>c</sup>, Baibiao Huang<sup>a</sup>, Peng Wang<sup>a,\*</sup>

<sup>a</sup> State Key Laboratory of Crystal Materials, Shandong University, Jinan 250100, China

<sup>b</sup> Shandong Yunhai Guochuang Innovative Technology Co., Ltd, Jinan 250101, China

<sup>c</sup> School of Physics, Shandong University, Jinan 250100, China

## ARTICLE INFO

### Keywords:

Lead-free perovskite

$\text{Cs}_3\text{Bi}_2\text{Br}_9$

$\text{TiO}_2$

C–H bonds activation

Photocatalysis

## ABSTRACT

Herein, a facile anti-solvent preparation strategy is proposed to fabricate lead-free halide perovskite  $\text{Cs}_3\text{Bi}_2\text{Br}_9$  with  $\text{TiO}_2$ , which boosts photocatalytic activation of  $\text{C}(\text{sp}^3)\text{--H}$  bonds in toluene oxidation.  $\text{TiO}_2$  not only works as nucleation center to reduce the particle size of perovskite, but could form type II heterojunction with  $\text{Cs}_3\text{Bi}_2\text{Br}_9$ , thus improving the photocatalytic performance of the  $\text{TiO}_2/\text{Cs}_3\text{Bi}_2\text{Br}_9$  composite. Under AM 1.5 G simulated sunlight irradiation, the optimal  $\text{TiO}_2/\text{Cs}_3\text{Bi}_2\text{Br}_9$  composite exhibits both high production rate ( $9692.5 \mu\text{mol g}^{-1} \text{h}^{-1}$ ) and selectivity (91 %) of benzaldehyde product. As verified by in-situ ESR, in-situ FT-IR and DFT calculations,  $\bullet\text{O}_2^-$  and  $\text{h}^+$  are demonstrated to be the main active species in this process. This work provides a new insight into the design of high-performance lead-free perovskite photocatalysts for organic synthesis.

## 1. Introduction

Halide perovskites represented by  $\text{MAPbI}_3$  and  $\text{CsPbBr}_3$  have attracted a lot of attention in solar cells [1,2], light-emitting diode [3], photoelectric detection [4] and so on due to their outstanding photoelectric conversion properties. The energy conversion efficiency of halide perovskite solar cells has rapidly increased from 3.8 % in 2009 to recently remarkable 27.7 % [5]. However, employing these materials as potential photocatalysts is seriously hindered due to their instability when exposing to moisture [6,7], which is contradictory with the common photocatalytic reactions systems in aqueous media, such as water splitting and organic waste degradation. To address this issue, Park et al. firstly reported the photocatalytic  $\text{H}_2$  evolution performance of  $\text{MAPbI}_3$  in its saturated HI solution [8]. The photocatalytic  $\text{H}_2$  evolution performances of perovskites in their saturated aqueous HI solution has been further investigated in the subsequent studies [9,10].

In addition to splitting haloid acid, exploring the applications of halide perovskites in organic phases may be a feasible approach, where organic solvent can effectively protect the halide perovskites from contacting with the humid external environment. So far, the

photocatalytic research of halide perovskites in organic phases has involved a variety of applications, including pollutant degradation [11], photocatalytic  $\text{CO}_2$  reduction [12,13] and organic synthesis [14,15]. Among them, utilizing halide perovskites for photocatalytic organic synthesis can take full advantage of their excellent photoelectric conversion performance, avoid the pollution and reduce the formation of by-products, which is meaningful for the actual chemical production. In particular, the selective activation of the saturated C–H bonds into high value added chemicals has full potential in the pharmaceutical, chemical and food industries [16–19]. However, this reaction also faces significant obstacles, one of which is the  $\text{C}(\text{sp}^3)\text{--H}$  bonds are very stable and require high energy to dissociate. Thermodynamic stability of  $\text{C}(\text{sp}^3)\text{--H}$  bonds makes it difficult to convert into useful oxygenated products [20]. In general, conventional methods of activating C–H bonds demand noble metal catalysts (i.e. Au and Pt), toxic and corrosive chemical oxidants (such as dichromate and permanganate) and harsh conditions, notably high temperature and pressure [21]. To overcome these obstacles, photocatalysis has been regarded as a promising method in selective activation of  $\text{C}(\text{sp}^3)\text{--H}$  bonds as a green and mild technology. Thus, there is a strong desire to utilize the excellent optical properties of halide

\* Corresponding author.

E-mail address: [pengwangicm@sdu.edu.cn](mailto:pengwangicm@sdu.edu.cn) (P. Wang).

<sup>1</sup> These authors contributed equally

perovskites for the selective photocatalytic of C–H bonds into value-added products [22]. Importantly, photocatalysis in organic phase can guarantee the stability of halide perovskites to the most extent.

Despite halide perovskites have shown huge potential for photocatalytic organic synthesis, it has to be acknowledged that the toxicity of lead has restricted their further development [23]. Researchers have tried to employ non-toxic elements like Sn and Ge in solar cell, but the resulting Sn or Ge based perovskites solar cell tend to be inferior to lead perovskites [24,25]. Since the  $\text{Bi}^{3+}$  and  $\text{Pb}^{2+}$  are isoelectronic and have similar ionic radii, Bi seems to be an appropriate alternative to Pb, which have aroused certain research in the photocatalysis [26,27]. However, the application of halide perovskites, especially bismuth-based halide perovskites in photocatalysis is still in its infancy, and the poor carrier separation efficiency of photocatalysts results in unsatisfactory performance [28,29]. In the traditional aqueous photocatalytic system, employing the energy band engineering to construct heterojunction is always an important method to promote the separation efficiency of photogenerated carriers [30]. Typically,  $\text{TiO}_2$  has been extensively studied due to its suitable band gap, high stability, low cost and non-toxic, which has been an outstanding choice for industrial production and basic research at present [31,32]. Especially, it has been widely used as an electron collection and transport material in solar cells, usually in the ingredient of compact layer (hole blocking layer) and porous layer (electron transport layer) [33]. Inspired from solar cells, it might be a suitable method to construct heterojunction of halide perovskite and  $\text{TiO}_2$  to improve the carrier lifetime. In particular, P25 has become our first choice owing to its high chemical purity and outstanding dispersion in liquid media [34,35]. The large specific surface area of P25 makes  $\text{TiO}_2$  have a stronger ability to capture the solution components (such as  $\text{O}_2$  and toluene) on its surface. In addition, it has excellent properties for many photocatalytic reactions and can be further functionalized [36]. Moreover, we find  $\text{TiO}_2$  can also serve as a nucleation site of perovskites and reduce the perovskites' size.

Halide perovskites can be effectively prepared by a variety of methods due to their low thermodynamic formation energies, including solid phase sintering, co-precipitation, anti-solvent method and so on [37]. Among these methods, anti-solvent assisted crystallization should be a simple and inexpensive way to obtain perovskite materials, and has received considerable attention in the preparation of solar cells [38]. This method can reduce the solubility of the specified solute and precipitate via adding a large amount of anti-solvent to a solvent system. The mechanism is to promote heterogeneous nucleation by producing transient local supersaturation. As for the synthesis of halide perovskites, the anti-solvent requires the miscibility with perovskites precursor solution and the insolubility of perovskites [39,40]. Meanwhile, the utilization of anti-solvent promotes rapid nucleation and is favorable in regulating grain growth and crystal nucleation [41]. In this work, we prepared the composite of lead-free perovskite  $\text{Cs}_3\text{Bi}_2\text{Br}_9$  with  $\text{TiO}_2$  employing a simple and facile anti-solvent method. This  $\text{TiO}_2/\text{Cs}_3\text{Bi}_2\text{Br}_9$  composite is shown to be a satisfactory photocatalyst for  $\text{C}(\text{sp}^3)\text{--H}$  bonds activation with high benzaldehyde production rate ( $9692.5 \mu\text{mol g}^{-1} \text{h}^{-1}$ ) and selectivity (about 91 %) under air mass 1.5G (AM 1.5G) simulated sunlight. This performance is excellent among the reported photocatalysts and thermal catalysts, and is far better than that of lead-based perovskite. Our work provides a strategy to explore the application of lead-free perovskites as photocatalysts, also offers an approach to promote their performance.

## 2. Experimental section

### 2.1. Materials and reagents

Dimethyl sulfoxide (DMSO), isopropanol and ethanol were purchased from Sinopharm Chemical Reagent. Bismuth bromide ( $\text{BiBr}_3$ , 98 %) was purchased from Macklin; Caesium bromide ( $\text{CsBr}$ , 99.9 %) was purchased from Aladdin.  $\text{TiO}_2$  is P25 powder purchased from Degussa.

All experiment reagents were analytical pure and without further purification.

### 2.2. Preparation of $\text{Cs}_3\text{Bi}_2\text{Br}_9$ (CBB) powders

Lead-free perovskite  $\text{Cs}_3\text{Bi}_2\text{Br}_9$  (CBB) was synthesized by a simple and facile anti-solvent precipitation method in the room temperature. In brief, 2 mmol  $\text{BiBr}_3$  and 3 mmol  $\text{CsBr}$  were dissolved in 5 mL DMSO with the assistance of ultrasound. Then 1 mL of prepared solution was added dropwise into a vigorously stirred 20 mL isopropanol, resulting in a light yellow suspension. Then the homogeneous mixture continued to stir for 2 h. The precipitate was filtered, then washed with isopropanol and ethanol several times and finally dried under vacuum at 80 °C overnight.

### 2.3. Preparation of $\text{CsPbBr}_3$ (CPB) powders

The preparation method of lead halide perovskite  $\text{CsPbBr}_3$  was consistent with that reported in the previous literature [42].

### 2.4. Preparation of $\text{TiO}_2/\text{Cs}_3\text{Bi}_2\text{Br}_9$ powders

The series of  $\text{TiO}_2/\text{CBB}$  samples were obtained by the same anti-solvent precipitation method. In a typical experiment, 100 mg  $\text{TiO}_2$  was first added to 20 mL isopropanol and then formed a homogeneous mixture under ultrasound assistance. Then, a certain  $\text{CsBr}/\text{BiBr}_3/\text{DMSO}$  precursor-solution was added dropwise into the vigorously stirred suspension. The mixture was stirred for 2 h vigorously. After that, the precipitate was filtered, washed with isopropanol and ethanol for several times and finally dried under vacuum at 80 °C overnight. Through adjusting the amount of  $\text{CsBr}/\text{BiBr}_3/\text{DMSO}$  precursor-solution dropped, a series  $\text{TiO}_2/\text{Cs}_3\text{Bi}_2\text{Br}_9$  composites with different weight ratios were obtained.

### 2.5. Materials characterization

The phases and compositions of the as-prepared samples were carried out by XRD measurements on a Rigaku SmartLab 9KW X-ray diffractometer equipped with  $\text{Cu K}\alpha$  irradiation. The surface morphologies and detailed structure of the samples were obtained using SEM (Hitachi S-4800). X-ray photoelectron spectroscopy (XPS) and in-situ XPS spectra were examined using Thermo Fisher ESCALAB 250XI to study the surface chemical compositions and states of samples, and the C 1s peak at 284.8 eV was used to calibrate the binding energies of various elements. UV–vis diffuse reflectance spectra (DRS) were measured by Shimadzu UV-2600 spectrophotometer equipped with an integrating sphere using 100 %  $\text{BaSO}_4$  as a reflectance standard to explore the optical absorption. The nitrogen adsorption/desorption isotherms of the obtained samples were recorded on a Kubo-X1000 apparatus to conduct the Brunauer-Emmett-Teller (BET) surface area. In-situ ESR spectra were obtained through JES FA200, where DMPO and TEMPO were used as spin-trapped reagents. The products were analyzed by GC-MS chromatography (GC-MS-QP2010, SH-Rtx-Wax column). In-situ diffuse reflectance infrared Fourier-transform spectroscopy (DRIFTS) were recorded through Nicolet IS50.

### 2.6. ESR measurements

The signals of  $\text{h}^+$  and  $\bullet\text{O}_2^-$  are measured by the following method. For  $\text{h}^+$ , we first dispersed the photocatalyst in toluene to prepare a dispersion solution with a concentration of 1 mg/mL with the assistance of ultrasound. Then, 100  $\mu\text{L}$  of the above dispersion solution was taken and mixed with a certain acetonitrile. After that, 200  $\mu\text{L}$  of TEMPO (2,2,6,6-Tetramethyl-1-piperidinyloxy) solution was put into the system (the concentration of TEMPO was 30 mM). TEMPO was the trapping agent to capture  $\text{h}^+$  radicals. Generally, the characteristic peaks of  $\text{TEMPO-h}^+$  with an intensity ratio of 1:1:1 could be observed under dark conditions.

When the system exposed to light irradiation, TEMPO would be consumed due to the photocatalysts could produce photo-generated holes, and then the intensity of the TEMPO- $h^+$  characteristic peaks would decrease accordingly. The decrease intensity could be used to assess the ability of photocatalysts to produce photo-generated holes. The new solution was mixed uniformly under ultrasound and taken out with a capillary tube. Then, the sealed capillary tube was put into the sample tube and finally measured with DJES FA200 to obtain the signal in dark. During illumination, the centrifuge tube was constantly shaken to prevent the obvious stratification of toluene and acetonitrile. Then solution was sampled with capillary tube and then collected signals after 3 min and 5 min of illumination. For  $\bullet O_2^-$ , the same 1 mg/mL dispersion solution was also prepared. Then, 100  $\mu$ L of the above dispersion solution was mixed with 100  $\mu$ L of DMPO (5,5-Dimethyl-1-Pyrroline N-Oxide) solution with a concentration of 100 mM, which DMPO was used as the trapping agent to capture  $\bullet O_2^-$  radicals. Under light irradiation, the DMPO would form DMPO- $\bullet O_2^-$  adducts with  $\bullet O_2^-$  when the photocatalysts had the capacity to generate  $\bullet O_2^-$  radicals. The characteristic peaks intensity (1:1:1:1) of DMPO- $\bullet O_2^-$  could be employed to study the capacity of the photocatalyst to generated  $\bullet O_2^-$  radicals. The specific test method under dark and illumination was the same as the above mentioned. The light source was provided by the 300 W Xe lamp (CEL-HXF300, Beijing CEAU Light, China) with an AM 1.5 cut-off filter.

## 2.7. Sample analysis

The catalytic activity of the sample for photocatalytic  $C(sp^3)-H$  bonds activation performance was evaluated at atmospheric pressure in a home-made two-neck quartz reactor equipped with a quartz window. A 300 W Xe-lamp (CEL-HXF300, Beijing CEAU Light, China) with an AM 1.5 cut-off filter was used as a light source for the photocatalytic experiment, and the irradiation density was 400 mW/cm<sup>2</sup>. In a common procedure, 5 mg of as-prepared photocatalyst was added to 5 mL of toluene in the reactor, then 100 mg of Na<sub>2</sub>SO<sub>4</sub> was added to remove the trace water produced during the reaction. The reaction temperature was maintained at 25 °C with a circulation cooling water system. Prior to irradiation, the system was bubbled with O<sub>2</sub> for 30 min, and then the system was sealed up. After 2 h irradiation, 0.2 mL of suspension was taken from the reactor, then 1  $\mu$ L of supernatant was analyzed using GC-MS after centrifugation at 12600 rpm for 2 min

## 2.8. Density functional theory (DFT) calculations

Density functional theory (DFT) calculations were carried out by using the Vienna Ab initio Simulation Package, in which the electron exchange-correlation energy was disposed by the Perdew-Burke-Ernzerhof (PBE) functional within the generalized gradient approximation (GGA). The mutual effect among electrons of cores and valence were executed by the projector augmented wave (PAW). The Brillouin zone was sampled by the  $3 \times 2 \times 1$  and  $1 \times 2 \times 1$  Monkhorst-Pack  $\Gamma$ -centered grids for the CBB-202 and CBB-202-TiO<sub>2</sub>-101 surface. The surface relaxation was implemented by a kinetics 400 eV cut off energy to the plane wave basis set. The relaxation threshold of surface optimization for force per atom and energy were set as 0.02 and  $10^{-5}$  eV. A 15 Å vacuum space was set to avoid the interaction come from the periodic boundary conditions. The adsorption energy of small molecules on catalyst surfaces is calculated by equation:

$$\Delta E_M = E_{\text{slab}+M} - E_{\text{slab}} - E_M$$

Where  $E_{\text{slab}+M}$  and  $E_{\text{slab}}$  are the total energy of with and without molecules adsorption on catalyst surfaces, and  $E_M$  represent the total energy of an isolated molecule in gas phase. The adsorption energy ( $E_{\text{ab}}$ ) of toluene were defined as:

$$E_{\text{ab}} = E(\text{sub}+\text{PhCH}_3) - E(\text{sub}) - E(\text{PhCH}_3)$$

Where  $E(\text{sub}+\text{PhCH}_3)$  and  $E(\text{sub})$  are the total energy of the system with and without PhCH<sub>3</sub>.  $E(\text{PhCH}_3)$  is the total energy of PhCH<sub>3</sub> molecules.

## 3. Results and discussion

### 3.1. Synthesis and Characterization of TiO<sub>2</sub>/CBB

The synthesis schematic of TiO<sub>2</sub>/Cs<sub>3</sub>Bi<sub>2</sub>Br<sub>9</sub> (CBB) is illustrated in Fig. S1 and the detailed preparation steps are shown in Experimental Section part. Figs. 1a, S2 and S3 reveals the XRD patterns of as-prepared samples. It can be seen that the prepared TiO<sub>2</sub>/CBB composite has the main diffraction peaks of TiO<sub>2</sub> and CBB, which reveals the anti-solvent method doesn't destroy their original structures. Meanwhile, the intensity of the characteristic peaks of CBB is increased with the increase of the CBB's weight ratio. The scanning electron microscopy (SEM) images of the above samples are exhibited in Fig. S4. The average particle size of pure CBB is about 1  $\mu$ m, while is about 100 nm in TiO<sub>2</sub>/CBB composite, indicating TiO<sub>2</sub> can serve as a nucleation site to reduce the perovskites' size. This result is further confirmed through subsequent UV-vis diffuse reflectance and PL spectra. Transmission electron microscopy (TEM) images of TiO<sub>2</sub>/CBB composite are described in Figs. 1b and S5. The lattice fringes spacings are calculated to be 0.31 nm and 0.35 nm, which are ascribed to the (112) and (101) crystallographic plane of CBB and TiO<sub>2</sub>, respectively [43,44]. Five elements of Ti, O, Cs, Bi and Br can be observed in the EDS spectrum of TiO<sub>2</sub>/CBB composite (Fig. S6), and Fig. S7 reveals the EDS mapping of these five elements. To further access the elemental composition and the elements chemical states on the surfaces of the obtained samples, X-ray photoelectron spectroscopy (XPS) spectra of TiO<sub>2</sub>/CBB composite are investigated in Fig. S8. The binding energy positions of all elements are consistent with those of elements in TiO<sub>2</sub> and CBB [45,46]. Meanwhile, the peaks of Cs, Bi and Br of TiO<sub>2</sub>/CBB have no significant difference shift with those of CBB, proving that the crystallization process has no effect on CBB structure. All these results demonstrate the successful preparation of composites.

### 3.2. Optical Properties of TiO<sub>2</sub>/CBB

We then record the Ultraviolet-visible diffuse reflectance spectra (DRS) of the obtained samples in Fig. 2a to study their optical properties. The bandgaps of pristine TiO<sub>2</sub> and CBB powder are found to be 3.32 eV and 2.63 eV, respectively (Fig. 2b). The absorption edge of the TiO<sub>2</sub>/CBB composite showed a slight blue shift compared with pure CBB. Correspondingly, the yellow degree of CBB is more obvious than that in TiO<sub>2</sub>/CBB composite (Fig. S9). This is due to the quantum confinement effect caused by the reduction of CBB's size [47]. Fig. S10 reveals the Nitrogen adsorption-desorption isotherms of the obtained samples. The BET specific surface areas are recorded in Table S1, where the BET specific surface areas of TiO<sub>2</sub>/CBB are larger than pure CBB, and decreases with the increase of the proportion of CBB. Steady-state photoluminescence (PL) spectra of CBB and TiO<sub>2</sub>/CBB composite are compared in Fig. 2c. The emission peak position of pure CBB is about 485 nm, while the emission peak of TiO<sub>2</sub>/CBB shows a slight blue shifted, which is in agreement with the above results. Fig. 2d shows the time-resolved photoluminescence (TRPL) spectra of CBB and TiO<sub>2</sub>/CBB composite. A three-exponential function is employed to fit the PL decay traces. The average PL decay times are summarized in Table S2. The average charge carrier lifetime for CBB is 2.78 ns, which increases to 4.06 ns for TiO<sub>2</sub>/CBB composite, illustrating that the charge carrier recombination in TiO<sub>2</sub>/CBB composite is efficiently suppressed. The PL and TRPL spectra of TiO<sub>2</sub> are shown in Fig. S11a and 11b. The average PL decay times are summarized in Table S3. The average charge carrier lifetime for TiO<sub>2</sub> is 1.78 ns, which is less than that of CBB and TiO<sub>2</sub>/CBB. Furthermore, the extension of carrier lifetime is conducive to the carriers transfer to the reaction interface, which implies that TiO<sub>2</sub>/CBB composite has better photocatalytic performance.

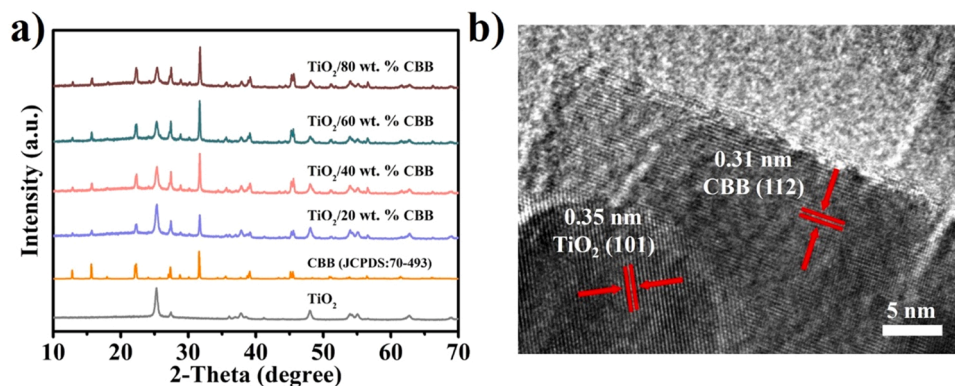


Fig. 1. (a) The XRD patterns of the obtained  $\text{TiO}_2/\text{CBB}$  composites with different CBB weight ratios. (b) HRTEM image of  $\text{TiO}_2/\text{CBB}$ .

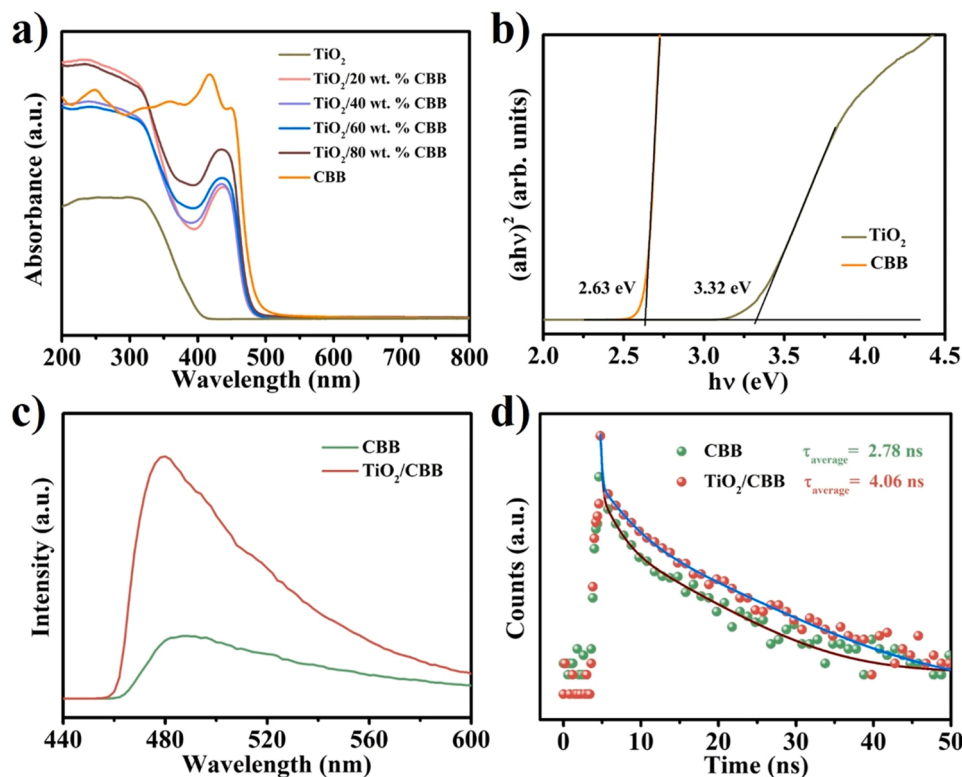


Fig. 2. (a) UV-vis diffuse reflectance spectra and (b) The  $(Ah\nu)^2$ - $h\nu$  plots of CBB and  $\text{TiO}_2$ . (c) Steady-state PL spectra of CBB and  $\text{TiO}_2/\text{CBB}$ . (d) PL decay spectra of CBB and  $\text{TiO}_2/\text{CBB}$  collected at the indicated emission wavelengths with 405 nm laser excitation light.

### 3.3. The photocatalytic performance

The photocatalytic performance of as-prepared  $\text{TiO}_2$ , CBB and  $\text{TiO}_2/\text{CBB}$  was evaluated for the activation of  $\text{C}(\text{sp}^3)\text{--H}$  bonds of the methyl group in toluene under light irradiation. Fig. S12 shows the schematic diagram of the measurement. The photocatalytic reaction equation is shown in Fig. 3a. During each experiment, a certain amount of  $\text{Na}_2\text{SO}_4$  was added to remove the trace water produced during the reaction (Fig. S13). The reaction temperature was maintained at 25 °C with a circulation cooling water system. Fig. 3b displays the selective oxidation of  $\text{C}(\text{sp}^3)\text{--H}$  bonds using  $\text{TiO}_2/\text{CBB}$  under different conditions. No product is detected in the dark, and same result is obtained under light irradiation without photocatalyst. This suggests that the activation of  $\text{C}(\text{sp}^3)\text{--H}$  bonds is driven by photocatalysis. Fig. 3c depicts the photo-oxidation of  $\text{C}(\text{sp}^3)\text{--H}$  bonds performance of  $\text{TiO}_2$ , CBB and  $\text{TiO}_2/\text{CBB}$  samples. The performance of pure  $\text{TiO}_2$  and CBB is general, and the

production rate of benzaldehyde in 2 h is  $649.8 \mu\text{mol g}^{-1} \text{h}^{-1}$  and  $2297.1 \mu\text{mol g}^{-1} \text{h}^{-1}$ , respectively. Whereas, it is gratifyingly that  $\text{TiO}_2/\text{CBB}$  composites show a substantial improvement.  $\text{TiO}_2/\text{CBB}$  60 wt. % shows the best performance among them and the production rate of benzaldehyde reaches  $9692.5 \mu\text{mol g}^{-1} \text{h}^{-1}$ , which is 14.9 and 4.2 times higher than that of pure phase, respectively. This result is superior to most photocatalysts and thermal catalysts reported so far (Table S4). To further verify the superiority of the prepared  $\text{TiO}_2/\text{CBB}$ , the photon absorption intensity, the specific extinction coefficient and optical thickness in the reactor of  $\text{TiO}_2$ , CBB and  $\text{TiO}_2/\text{CBB}$  are also obtained in toluene suspensions according to the methods reported in the reference [48–54]. As revealed in Fig. S14a, the photon absorption intensities of  $\text{TiO}_2$ , CBB and  $\text{TiO}_2/\text{CBB}$  in 5 mL toluene solution are measured to be  $269.1 \text{ mW/cm}^2$ ,  $274.8 \text{ mW/cm}^2$  and  $296.4 \text{ mW/cm}^2$ , respectively. The photon absorption intensity of  $\text{TiO}_2/\text{CBB}$  only increases slightly compared with those of  $\text{TiO}_2$  and CBB, which indicates that  $\text{TiO}_2/\text{CBB}$



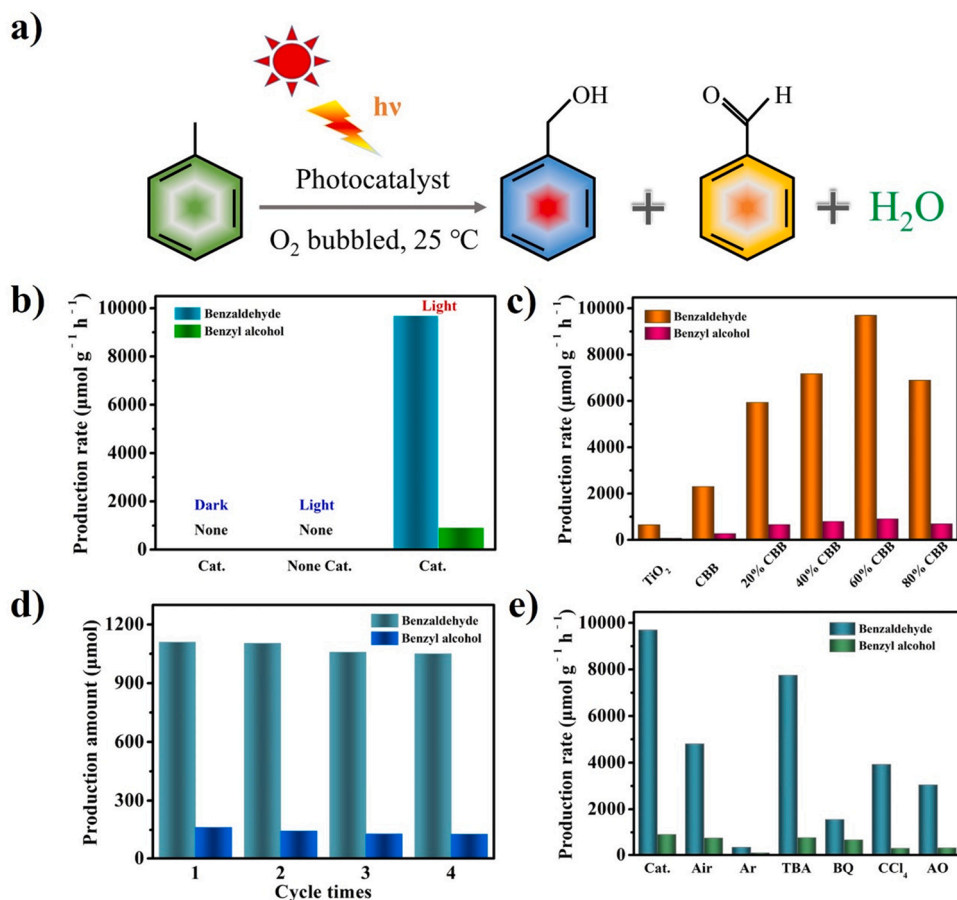


**Fig. 3.** (a) Reaction equation for photocatalytic oxidation of toluene. (b) The photocatalytic performance of TiO<sub>2</sub>/CBB under different conditions. (c) The photocatalytic performance of TiO<sub>2</sub>, CBB, and series TiO<sub>2</sub>/CBB composites in 2 h light irradiation. (d) The cycle experiment test of TiO<sub>2</sub>/CBB (50 mg of photocatalyst). (e) The photocatalytic performance of TiO<sub>2</sub>/CBB under different conditions and in the presence of different radical scavengers.

has better photocatalytic performance under the condition of controlling the same total photon absorption rate. Moreover, as shown in Fig. S14b, the specific extinction coefficients of TiO<sub>2</sub>, CBB and TiO<sub>2</sub>/CBB are calculated by the following equations:

$$\beta_{\lambda} = \frac{2.303EXT_{\lambda}}{L} \quad (1)$$

$$\beta_{\lambda}^* = \frac{\beta_{\lambda}}{C_{cat}} \quad (2)$$

$$\beta^* = \frac{\int_{\lambda_{min}}^{\lambda_{max}} \beta_{\lambda}^* I_{\lambda} d\lambda}{\int_{\lambda_{min}}^{\lambda_{max}} I_{\lambda} d\lambda} \quad (3)$$

where  $\beta_{\lambda}$ ,  $EXT_{\lambda}$  and  $L$  (10 mm in this work) are the extinction coefficient, extinction of an incident beam and the path-length of the quartz cell, respectively.  $\beta_{\lambda}^*$ ,  $C_{cat}$ ,  $\beta^*$  and  $I_{\lambda}$  are the specific extinction coefficient, the catalyst mass concentration, the spectral-averaged specific extinction coefficient and the useful spectrum of the incident irradiation, respectively. The estimated spectral-averaged specific extinction coefficients  $\beta^*$  of TiO<sub>2</sub>, CBB and TiO<sub>2</sub>/CBB in the region from 300 to 500 nm are 585.3 m<sup>2</sup> kg<sup>-1</sup>, 332.5 m<sup>2</sup> kg<sup>-1</sup> and 33.9 m<sup>2</sup> kg<sup>-1</sup>, respectively. Thus, the optical thickness  $\tau$  in the reactor can be defined by the following equation:

$$\tau = \beta^* C_{cat} L$$

where  $\beta^*$ ,  $C_{cat}$  and  $L$  represent the spectral-averaged specific extinction coefficient, catalyst mass concentration and the characteristic length for the extinction of the light inside the reactor (the depth of a

5 mL toluene suspension in the reactor in this work, which is 0.006 m), respectively. According to the obtained  $\beta^*$  and  $C_{cat}$  (1 g L<sup>-1</sup>), the optical thickness  $\tau$  of TiO<sub>2</sub>, CBB and TiO<sub>2</sub>/CBB suspensions in the reactor are found to be 3.5, 2.0 and 0.2, respectively. Meanwhile, a fair comparison among TiO<sub>2</sub>, CBB and TiO<sub>2</sub>/CBB photocatalysts are further carried out via controlling the mass concentration of the catalysts at 0.57 g L<sup>-1</sup>, 1 g L<sup>-1</sup> and 10 g L<sup>-1</sup>, respectively. Fig. S15 describes the corresponding results. The yield of benzaldehyde in TiO<sub>2</sub>/CBB is much higher than that in TiO<sub>2</sub> and CBB, which indicates that TiO<sub>2</sub>/CBB can exhibit significantly enhanced photocatalytic performance at equal optical thickness  $\tau$ . In addition, control experiment shows that CsPbBr<sub>3</sub> has no ability to photo-oxidize toluene (Fig. S16), which might attributed to the large particle size of CsPbBr<sub>3</sub> (Fig. S17). Moreover, CsPbBr<sub>3</sub>/TiO<sub>2</sub> is also investigated. It can be seen in Fig. S18 that CsPbBr<sub>3</sub>/TiO<sub>2</sub> has the ability to activate the C(sp<sup>3</sup>)-H bond in toluene, but its photocatalytic oxidation performance is far less than that of TiO<sub>2</sub>/CBB (the production rate of benzaldehyde of CsPbBr<sub>3</sub>/TiO<sub>2</sub> is 1527.8 μmol g<sup>-1</sup> h<sup>-1</sup>). This result proves that lead-free halide perovskite CBB has better properties than lead-based halide perovskite CsPbBr<sub>3</sub>. Meanwhile, it should be noted that certain amount benzyl alcohol is also detected as the main side product (904.9 μmol g<sup>-1</sup> h<sup>-1</sup>), but the selectivity of benzaldehyde still reaches about 91 % (Fig. S19). Such high selectivity of benzaldehyde is more significant owing to the chemical value of benzaldehyde is higher than benzyl alcohol in the actual chemical production. To directly demonstrate that the obtained TiO<sub>2</sub>/CBB composite has excellent photocatalytic performance, we next test the performance of TiO<sub>2</sub>/CBB photocatalyst in sunlight on a sunny day in Jinan. As shown in Fig. S20, the production amount of benzaldehyde achieves 590 μmol under 5 h of sunlight irradiation (From 10:30–15:30). The yield reached its highest in

the hour of 12:30 – 13:30, coinciding with sunlight conditions. The toluene conversion rate can reach to 1.4 % molar ratio. In addition, the photocatalyst remains satisfactory performance after four cycles of experiments (Fig. 3d), indicating that  $\text{TiO}_2/\text{CBB}$  photocatalyst has good stability and practical application prospect, which is fully comparable to most of the existing perovskite photocatalysts (Table S5). In order to further explore the stability of the  $\text{TiO}_2/\text{CBB}$  during photocatalytic C(sp<sup>3</sup>)–H bond activation process, we perform the XRD, SEM images, UV–vis DRS and IR spectra of the  $\text{TiO}_2/\text{CBB}$  after light irradiation. As shown in the Fig. S21a, the diffraction peaks of  $\text{Na}_2\text{SO}_4$  appears in the XRD patterns of  $\text{TiO}_2/\text{CBB}$  after the reaction, while the position of other diffraction peaks have no change compared with those before reaction. This is because  $\text{Na}_2\text{SO}_4$  is difficult to separate from the sample after light irradiation as a water-trapping agent. A similar phenomenon can be observed in the IR spectra after the reaction (Fig. S21b). Figs. S22 and S23 reveals the SEM images and UV–Vis DRS before and after photocatalytic reaction. The morphology and absorption spectrum and of the photocatalyst after illumination are consistent with the initial sample. All these characterizations exhibit that the  $\text{TiO}_2/\text{CBB}$  has good stability for photocatalytic C(sp<sup>3</sup>)–H bond activation.

### 3.4. In-situ ESR spectra analysis

To access the active species and photocatalytic reaction mechanism in the activation of C(sp<sup>3</sup>)–H bonds of the methyl in toluene, series of control experiments are carried out under different conditions. As presented in Fig. 3e, the production rate of benzyl alcohol and benzaldehyde decreased obviously when  $\text{O}_2$  is not bubbled. The transformation of toluene is almost entirely prohibited when Ar is used instead of  $\text{O}_2$ , which confirms that the existence of  $\text{O}_2$  atmosphere is the necessary condition for driving the selective oxidation from toluene to benzyl alcohol and benzaldehyde. Experiments in the presence with different scavengers are also investigated. Tert-butanol (TBA), benzoquinone

(BQ),  $\text{CCl}_4$ , and ammonium oxalate (AO) are employed as the scavengers of hydroxyl radical ( $\bullet\text{OH}$ ), superoxide radical ( $\bullet\text{O}_2^-$ ), electrons ( $e^-$ ) and photo-generated holes ( $h^+$ ), respectively. When benzoquinone is added as a scavenger for  $\bullet\text{O}_2^-$ , the conversion of toluene is obviously inhibited. This result manifests that  $\bullet\text{O}_2^-$  plays an enormous role in the selective oxidation of toluene, and  $\bullet\text{O}_2^-$  is the main active species for activating C(sp<sup>3</sup>)–H bonds. In addition, trapped experiments of  $e^-$  and  $h^+$  also display that the transformation of toluene is restrained to varying degrees with the addition of AO and  $\text{CCl}_4$ . These experiments preliminarily demonstrate that  $h^+$  and  $\bullet\text{O}_2^-$  do exert an enormous impact on the toluene selective oxidation. To further directly verify the involved reactive species during the reaction process, in-situ electron spin resonance (ESR) technique is then performed by using 5,5-Dimethyl-1-Pyrroline N-Oxide (DMPO) and 2,2,6,6-Tetramethyl-1-piperidinyloxy (TEMPO) as spin-trapping agents. As depicted in Figs. 4a and S24, no obvious signal is found under dark conditions. Nevertheless, four characteristic peaks appear under light irradiation, corresponding to the characteristic peaks of the DMPO- $\bullet\text{O}_2^-$  adduct. The intensities of the peaks increase with the enhancement of irradiation time. The signal intensity of  $\text{TiO}_2/\text{CBB}$  is higher than that of  $\text{TiO}_2$  and CBB in the same time (Fig. 4b), which is consistent with their performance results, indicating that more  $\bullet\text{O}_2^-$  species are generated via  $\text{TiO}_2/\text{CBB}$  within a certain time. Furthermore, there are three characteristic peaks of spin-trapped TEMPO- $h^+$  under dark (Fig. 4c). These peaks intensities recede dramatically when exposed to light irradiation, and the intensities decrease with light irradiation. Among the three  $\text{TiO}_2$ , CBB and  $\text{TiO}_2/\text{CBB}$  photocatalysts, TEMPO- $h^+$  characteristic peaks have similar intensities under initial conditions, but after a period time of illumination, the intensity of  $\text{TiO}_2/\text{CBB}$  is lower than that of  $\text{TiO}_2$  and CBB (Fig. 4d). That means more holes in  $\text{TiO}_2/\text{CBB}$  are being consumed in the same time. In-situ ESR spectra show that the synergistic effect between  $h^+$  and  $\bullet\text{O}_2^-$  species makes the conversion of toluene, and  $\text{TiO}_2/\text{CBB}$  has higher photo-generated electron-hole pairs separation efficiency.

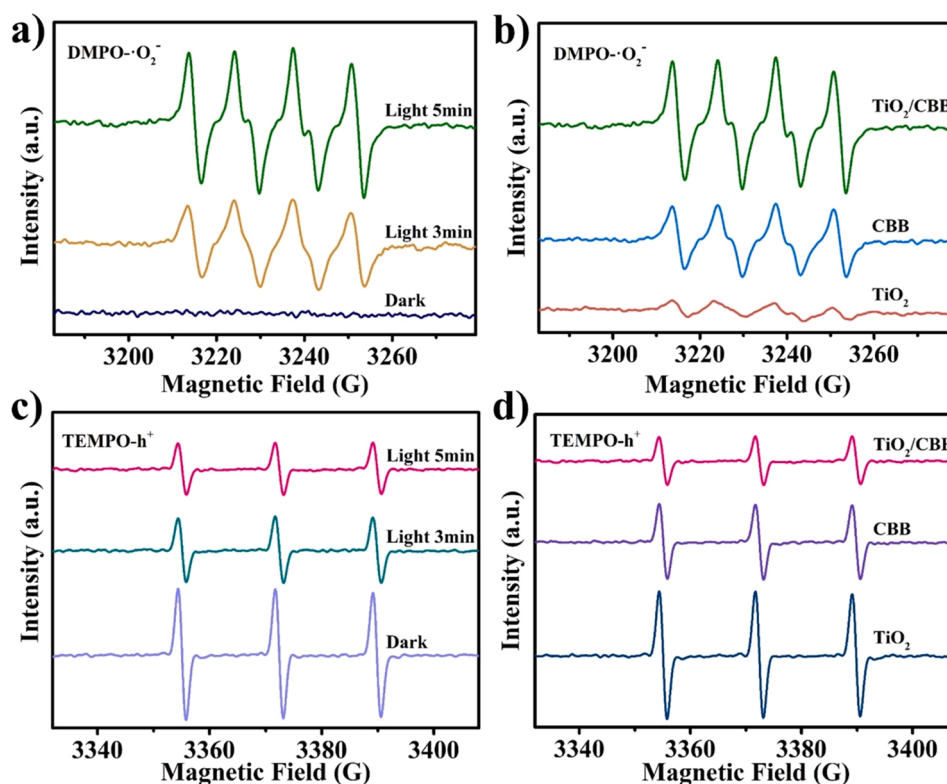


**Fig. 4.** In-situ ESR spectra of radical adducts trapped by (a) DMPO ( $\bullet\text{O}_2^-$ ) and (c) TEMPO ( $h^+$ ) in  $\text{TiO}_2/\text{CBB}$  dispersion in the darkness and light irradiation. Comparison of the (b) DMPO ( $\bullet\text{O}_2^-$ ) and (d) TEMPO ( $h^+$ ) ESR signal intensities of the  $\text{TiO}_2$ , CBB and  $\text{TiO}_2/\text{CBB}$  samples after the same illumination time.

### 3.5. Proposed mechanism

In order to identify the mechanism of photocatalytic activation of C (sp<sup>3</sup>)–H bonds in toluene by TiO<sub>2</sub>/CBB composite, we collected the ultraviolet photoelectron spectrometer (UPS) spectra of TiO<sub>2</sub> and CBB (Fig. S25). The actual valance band maximum (VBM) and the conduction band minimum (CBM) of TiO<sub>2</sub> and CBB are further calculated. The VB energy (E<sub>VB</sub>) of TiO<sub>2</sub> and CBB can be carried out by making the difference between the excitation energy (21.22 eV) and the width of the He I UPS spectrum. Meanwhile, according to the formula of  $E_g = E_{VB} - E_{CB}$  and the relationship of 0 V vs. NHE equal to  $-4.44$  eV vs. vacuum energy level, the VBM and CBM of TiO<sub>2</sub> are located at 2.96 eV and  $-0.36$  eV, while the VBM and CBM are located at 2.19 eV and  $-0.44$  eV for CBB, respectively (Fig. 5a) [55]. The appropriate energy bands between TiO<sub>2</sub> and CBB can make them form an II-type heterostructure when they are in contact [56,57]. Due to the electrons flow, positive charges and negative charges are effectively separated, resulting in a built-in electric field [30]. To verify the charge transfer mechanism between TiO<sub>2</sub> and CBB, ESR analysis was also used to explore the direction of electron transfer. As shown in Fig. S26a, DMPO is used as the trapping agent to capture  $\bullet$ OH radicals. It can be seen that no signal is observed under dark conditions. For TiO<sub>2</sub>/CBB, the intensity of DMPO- $\bullet$ OH characteristic peaks is higher than the sum of pure CBB and TiO<sub>2</sub> when exposed to light, which indicates more  $\bullet$ OH is generated in the composite under the light irradiation. Meanwhile, DMPO is also used to capture  $\bullet$ O<sub>2</sub> in Fig. S26b. Similar to the signal of DMPO- $\bullet$ OH, no signal is observed under dark conditions. Moreover, TiO<sub>2</sub>/CBB shows stronger DMPO- $\bullet$ O<sub>2</sub> signal under light irradiation than pure CBB and TiO<sub>2</sub>, which reveals that more photo-generated electrons are appeared in TiO<sub>2</sub>/CBB than those of TiO<sub>2</sub> and CBB. Notably, both single CBB and TiO<sub>2</sub> component can generate  $\bullet$ OH and  $\bullet$ O<sub>2</sub>, and the signal intensity of DMPO- $\bullet$ OH and DMPO- $\bullet$ O<sub>2</sub> in TiO<sub>2</sub>/CBB is much higher than those of CBB and TiO<sub>2</sub>. This indicates that TiO<sub>2</sub>/CBB has a faster photo-generated

electron hole separation efficiency. Moreover, the photo-generated holes was further verified through ESR spectra in Fig. S26c. The characteristic peaks intensity (1:1:1) of TEMPO-h<sup>+</sup> of TiO<sub>2</sub>/CBB is lower than that of TiO<sub>2</sub> and CBB, which means TiO<sub>2</sub>/CBB produces more photo-generated holes at the same irradiation time. These measurements prove that the transfer of photo-generated electrons and holes in TiO<sub>2</sub>/CBB is a type II process. In addition, surface photovoltage spectroscopy is also carried out in Fig. S26d, and the local electric field intensity of TiO<sub>2</sub>/CBB is significantly higher than that of TiO<sub>2</sub> and CBB. The stronger SPV response comes from more efficient separation of photo-generated charge carriers, thus the local electric field is further enhanced [58]. This phenomenon further proves that TiO<sub>2</sub> can effectively promote the separation of photo-generated carriers as an electron transport material and improve the photocatalytic performance.

Surface photoexcited electron-hole pairs will be generated when TiO<sub>2</sub>/CBB composite is exposed to light irradiation. The photo-generated electrons in the conduction band (CB) of CBB prefer to transfer to the TiO<sub>2</sub>, rather than recombine with the photo-generated hole in the valence band (VB) of CBB. Moreover, the photo-generated holes flow from the VB of TiO<sub>2</sub> to the VB of CBB, and react directly with the adsorbed toluene. Meanwhile, the anti-solvent method can actually reduce the size of perovskite and promote more reaction sites. It is the combination of these factors that makes the TiO<sub>2</sub>/CBB photocatalyst has excellent activity. The photoelectrochemical properties measurements were examined to study the separation ability of photo-generated carriers. Fig. 5b manifests the transient photocurrent response of prepared CBB, TiO<sub>2</sub> and TiO<sub>2</sub>/CBB thin films under AM 1.5 light irradiation in dichloromethane solution containing 0.1 M tetrabutylammonium hexafluorophosphate (TBAPF<sub>6</sub>) at 0.5 V versus Ag/AgCl electrode. Clearly, the TiO<sub>2</sub>/CBB exhibits a larger photocurrent density than pure CBB and TiO<sub>2</sub> when light hits the sample surface. This result exhibits that more photo-generated carriers are gathered on the surface of the TiO<sub>2</sub>/CBB thin film electrode than CBB and TiO<sub>2</sub>, and the

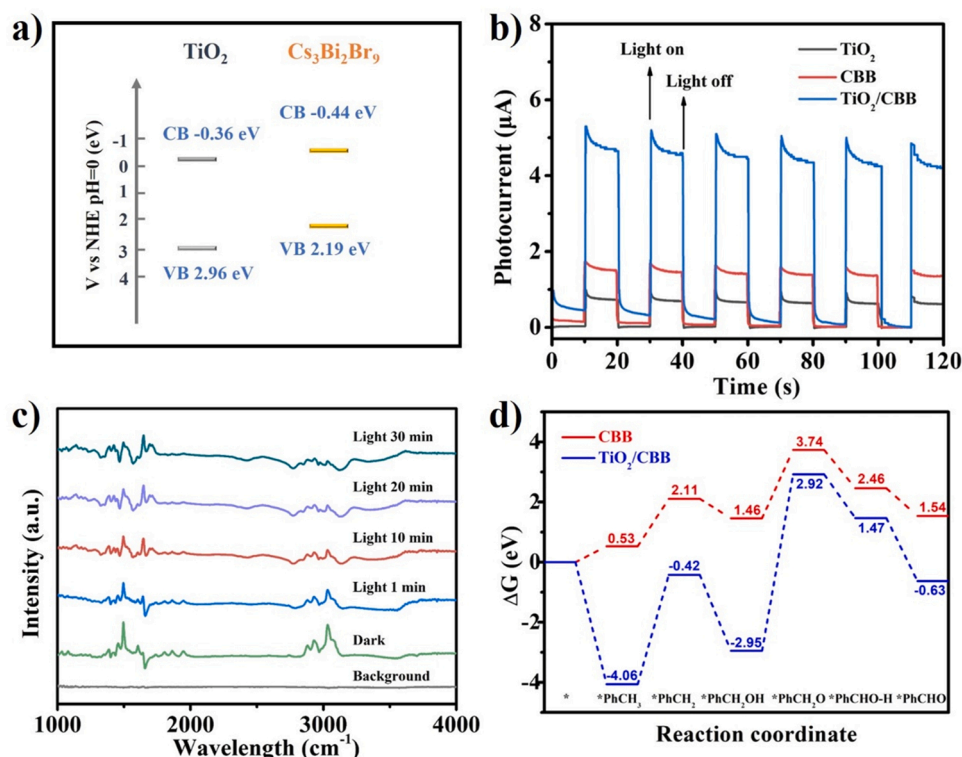


**Fig. 5.** (a) Schematic band diagram of TiO<sub>2</sub> and CBB. (b) Transient photocurrent responses of CBB and TiO<sub>2</sub>/CBB measured at 0.5 V versus Ag/AgCl electrode in dichloromethane solution containing 0.1 M tetrabutylammonium hexafluorophosphate (TBAPF<sub>6</sub>) as electrolyte solution. (c) In situ DRIFTS spectra of TiO<sub>2</sub>/CBB under reaction operation. (d) Gibbs free energy diagrams of photocatalytic toluene oxidation for CBB and TiO<sub>2</sub>/CBB.

photogenerated electron-hole pairs can be easily separated in TiO<sub>2</sub>/CBB sample. Fig. S27 presents the electrochemical impedance spectra (EIS) results of above samples measured in the same electrolyte. Accordingly, TiO<sub>2</sub>/CBB has smaller impedance than that of CBB and TiO<sub>2</sub>, which also shows that TiO<sub>2</sub>/CBB has a more efficient electron-hole separation and a higher rapid charge transfer capability. In-situ diffuse reflectance infrared Fourier-transform spectroscopy (DRIFTS) measurements were used to track the specific pathway of C(sp<sup>3</sup>)-H bonds activation under reaction operation. The toluene and O<sub>2</sub> gas mixture were passed into the in-situ pool for 20 min, and then the in-situ pool was sealed and illuminated. As shown in Fig. 5d, the stretching vibration of aromatic ring can be detected at 3039 cm<sup>-1</sup> and the C-H bonds stretching vibration from the toluene methyl group can be observed at 2927 cm<sup>-1</sup> before irradiation [59]. The intensities of these peaks reduce continuously with the irradiation time, indicating that toluene is involved in the reaction. Meanwhile, two peaks at 1058 cm<sup>-1</sup> and 1422 cm<sup>-1</sup> appear and rise with light duration, corresponding to C-O stretching vibration and CH<sub>2</sub> bonds deformation vibration of benzyl alcohol [60]. Peaks of association hydroxyl and free hydroxyl groups are also discovered at 3222 cm<sup>-1</sup> and 3618 cm<sup>-1</sup> [61,62]. Besides, a time-dependent increase peak at 1696 cm<sup>-1</sup> is witnessed with illumination time, which can be attributed to the carbonyl group of benzaldehyde [63,64]. Meanwhile, ESR spectra shows six characteristic peaks of DMPO-carbon center free radicals adducts under light irradiation, which demonstrates that the carbon center radical is also an important intermediate in the photocatalysis process (Fig. S28).

In addition, we studied the mechanism of photocatalytic C(sp<sup>3</sup>)-H bond activation through density functional theory (DFT) calculation. After optimization, the adsorption energies of CBB and TiO<sub>2</sub>/CBB for toluene were -0.09 eV and -4.68 eV, respectively. The negative adsorption energy of TiO<sub>2</sub>/CBB indicates that the formation of heterostructure is beneficial to the adsorption of toluene molecules. Moreover, TiO<sub>2</sub>/CBB has a larger BET specific surface area than CBB, thus it can provide more adsorption sites, which are conducive to the activation of adsorbed toluene and subsequent interaction with photo-generated carriers to form reaction intermediates. In addition, the specific oxidation steps of toluene were also carried out by DFT calculation. The interaction models of CBB and TiO<sub>2</sub>/CBB with each intermediate in the photocatalytic process are obtained in Table. S6. The corresponding Gibbs free energy ( $\Delta G$ ) for each reaction steps is calculated and shown in Fig. 5d. It can be seen that the formation of benzyl group (\*PhCH<sub>2</sub>) from toluene is considered as the rate-determining step of photocatalytic oxidation of toluene, and TiO<sub>2</sub>/CBB has lower benzyl formation energy than that of CBB. After a dehydrogenation process, benzyl reacts with the generated •O<sub>2</sub><sup>-</sup> to generate \*PhCH<sub>2</sub>OH. The benzaldehyde is finally formed from generated \*PhCH<sub>2</sub>OH through two continuous dehydrogenation processes, which the O-H bond in the OH group and the C-H bond in the methyl group break, respectively [65].

Based on the above results, we propose the following possible reaction mechanism of toluene oxidation. The larger BET specific surface area and lower adsorption energy of TiO<sub>2</sub>/CBB are conducive to the adsorption of toluene molecules on the photocatalyst on the dark conditions. When the system is exposed to light, the photocatalyst generates electrons and holes under the excitation of light. For TiO<sub>2</sub>/CBB photocatalyst, TiO<sub>2</sub> can effectively promotes the separation of photogenerated carriers as an electron transport material and promote the lifetime of carriers. The photo-generated electrons further react with the oxygen dissolved in toluene to generate •O<sub>2</sub><sup>-</sup>. The adsorbed toluene is further activated to generate benzyl radical via photo-generated holes, which is the rate-determining step of the whole reaction. •O<sub>2</sub><sup>-</sup> react with benzyl radicals, and benzyl alcohol and benzaldehyde are finally produced. TiO<sub>2</sub>/CBB has more effective photo-generated carriers separation efficiency, and overcomes the low energy barrier during the photocatalytic process. Therefore, TiO<sub>2</sub>/CBB shows a better photocatalytic performance.

## 4. Conclusion

In summary, we prepared TiO<sub>2</sub>/Cs<sub>3</sub>Bi<sub>2</sub>Br<sub>9</sub> photocatalyst through a simple anti-solvent method, which can availablely reduce the size of perovskite. This composite shows a satisfactory performance for C(sp<sup>3</sup>)-H bonds activation. The production amount of benzaldehyde achieves 590  $\mu$ mol under 5 h of sunlight irradiation. This composite is also highly stable, showing no significant decrease in the catalytic activity after four cycles of experiments. We think this work not only provides a strategy to explore the application of lead-free perovskite as photocatalysts, but also offers an approach to promote their performance.

## CRedit authorship contribution statement

**Zihao Cui:** Formal analysis, Methodology, Data curation, Resources, Investigation, Writing - original draft, Writing - review & editing. **Qianqian Zhang:** Validation, Data curation, Investigation. **Hui Fu:** Methodology, Investigation. **Qihao Liu:** Investigation, Resources. **Xiaolei Liu:** Methodology, Validation. **Yaqiang Wu:** Methodology, Validation. **Peng Gao:** Methodology. **Zeyan Wang:** Methodology. **Zhaoke Zheng:** Validation. **Hefeng Cheng:** Investigation. **Yuanyuan Liu:** Investigation, Validation. **Ying Dai:** Software, Validation. **Baibiao Huang:** Conceptualization, Supervision, Project administration, Funding acquisition. **Peng Wang:** Conceptualization, Supervision, Writing - review & editing, Project administration, Funding acquisition.

## Declaration of Competing Interest

The authors declare that they have no known competing financial interests or personal relationships that could have appeared to influence the work reported in this paper.

## Data Availability

No data was used for the research described in the article.

## Acknowledgements

This work was financially supported by the National Natural Science Foundation of China (21832005, 22072071, 51972195, 21972078, 2210020454 and 22072072), National Natural Science Foundation of Shandong Province (ZR2020JQ06, ZQ2020QB058 and ZR2022ZD25), National Key Research and Development Program of China (2020YFA0710301), and China Postdoctoral Science Foundation (2020M672055 and 2021M691901). In addition, Zihao Cui would like to thank Lawyer Rengang Zhang for his help and wish him in good health.

## Appendix A. Supporting information

Supplementary data associated with this article can be found in the online version at doi:10.1016/j.apcatb.2023.122812.

## References

- [1] H. Min, M. Kim, S.U. Lee, H. Kim, G. Kim, K. Choi, J.H. Lee, S.I. Seok, Efficient, stable solar cells by using inherent bandgap of a-phase formamidinium lead iodide, *Science* 366 (2019) 749–753.
- [2] R. Lin, J. Xu, M. Wei, Y. Wang, Z. Qin, Z. Liu, J. Wu, K. Xiao, B. Chen, S.M. Park, G. Chen, H.R. Atapattu, K.R. Graham, J. Xu, J. Zhu, L. Li, C. Zhang, E.H. Sargent, H. Tan, All-perovskite tandem solar cells with improved grain surface passivation, *Nature* 603 (2022) 73–78.
- [3] Z.K. Tan, R.S. Moghaddam, M.L. Lai, P. Docampo, R. Higler, F. Deschler, M. Price, A. Sadhanala, L.M. Pazos, D. Credgington, F. Hanusch, T. Bein, H.J. Snaith, R. H. Friend, Bright light-emitting diodes based on organometal halide perovskite, *Nat. Nanotechnol.* 9 (2014) 687–692.
- [4] M.I. Saidaminov, V. Adinolfi, R. Comin, A.L. Abdelhady, W. Peng, I. Dursun, M. Yuan, S. Hoogland, E.H. Sargent, O.M. Bakr, Planar-integrated single-crystalline perovskite photodetectors, *Nat. Commun.* 6 (2015) 8724.



- [5] T. Duong, H. Pham, T.C. Kho, P. Phang, K.C. Fong, D. Yan, Y. Yin, J. Peng, M. A. Mahmud, S. Gharibzadeh, B.A. Nejand, I.M. Hossain, M.R. Khan, N. Mozaffari, Y. Wu, H. Shen, J. Zheng, H. Mai, W. Liang, C. Samundsett, M. Stocks, K. McIntosh, G.G. Andersson, U. Lemmer, B.S. Richards, U.W. Paetzold, A. Hoetzold, Y. Liu, D. Macdonald, A. Blakers, J. Wengersldt, T. White, K. Weber, K. Catchpole, High Efficiency Perovskite crystalline perovskite photodetectorsskivation Coating versus Bulk Incorporation of 2D Perovskite, *Adv. Energy Mater.* 10 (2020) 1903553.
- [6] Z. Song, A. Abate, S.C. Wathage, G.K. Liyanage, A.B. Phillips, U. Steiner, M. Graetzel, M.J. Heben, Perovskite solar cell stability in humid air: partially reversible phase transitions in the  $\text{PbI}_2\text{-er}_3\text{NH}_3\text{I}^+\text{Hr}_2\text{O}$  system, *Adv. Energy Materials* 6 (2016) 1600846.
- [7] S.K. Balakrishnan, P.V. Kamat, Ligand assisted transformation of cubic  $\text{CsPbBr}_3$  nanocrystals into two-dimensional  $\text{CsPb}_2\text{Br}_5$  nanosheets, *Chem. Mater.* 30 (2017) 74–78.
- [8] S. Park, W.J. Chang, C.W. Lee, S. Park, H.-Y. Ahn, K.T. Nam, Photocatalytic hydrogen generation from hydriodic acid using methylammonium lead iodide in dynamic equilibrium with aqueous solution, *Nature Energy* 2 (2016) 16185.
- [9] Y. Wu, Q. Wu, Q. Zhang, Z. Lou, K. Liu, Y. Ma, Z. Wang, Z. Zheng, H. Cheng, Y. Liu, Y. Dai, B. Huang, P. Wang, An organometal halide perovskite supported Pt single-atom photocatalyst for  $\text{H}_2$  evolution, *Energy Environ. Sci.* 15 (2022) 1271–1281.
- [10] X. Zhao, S. Chen, H. Yin, S. Jiang, K. Zhao, J. Kang, P.F. Liu, L. Jiang, Z. Zhu, D. Cui, P. Liu, X. Han, H.G. Yang, H. Zhao, Perovskite microcrystals with intercalated monolayer  $\text{MoS}_2$  nanosheets as advanced photocatalyst for solar-powered hydrogen generation, *Matter* 3 (2020) 935–949.
- [11] Z. Zhang, Y. Liang, H. Huang, X. Liu, Q. Li, L. Chen, D. Xu, Stable and highly efficient photocatalysis with lead-free double-perovskite of  $\text{Cs}_2\text{AgBiBr}_6$ , *Angew. Chem. Int. Ed.* 58 (2019) 7263–7267.
- [12] W.T. Man Ou, Shengming Yin, Weinan Xing, Shuyang Wu, Haojing Wang, Shipeng Wan, Qin Zhong, Rong Xu, Amino-assisted anchoring of  $\text{CsPbBr}_3$  perovskite quantum dots on porous  $\text{g-C}_3\text{N}_4$  for enhanced photocatalytic  $\text{CO}_2$  reduction, *Angew. Chem. Int. Ed.* 130 (2018) 13758–13762.
- [13] Y.F. Xu, M.Z. Yang, B.X. Chen, X.D. Wang, H.Y. Chen, D.B. Kuang, C.Y. Su, A  $\text{CsPbBr}_3$  Perovskite Quantum Dot/Graphene Oxide Composite for Photocatalytic  $\text{CO}_2$  Reduction, *J. Am. Chem. Soc.* 139 (2017) 5660–5663.
- [14] Z. Hong, W.K. Chong, A.Y.R. Ng, M. Li, R. Ganguly, T.C. Sum, H.S. Soo, Hydrophobic metal halide perovskites for visible-light photoredox C-C bond cleavage and dehydrogenation catalysis, *Angew. Chem. Int. Ed.* 58 (2019) 3456–3460.
- [15] K. Chen, X. Deng, G. Dodekatos, H. Tuysuz, Photocatalytic polymerization of 3,4-ethylenedioxythiophene over cesium lead iodide perovskite quantum dots, *J. Am. Chem. Soc.* 139 (2017) 12267–12273.
- [16] J.A. Labinger, J.E. Bercaw, Understanding and exploiting C-H bond activation, *Nature* 417 (2002) 507–514.
- [17] F.Ra.C. Punta, Free radical functionalization of organic compounds catalyzed by N-hydroxyphthalimide, *Chem. Rev.* 107 (2007) 3800–3842.
- [18] L. Lin, Q. Zhang, Y. Ni, L. Shang, X. Zhang, Z. Yan, Q. Zhao, J. Chen, Rational design and synthesis of two-dimensional conjugated metal-organic polymers for electrocatalysis applications, *Chem* 8 (2022) 1822–1854.
- [19] A. Huang, Y. Ma, J. Peng, L. Li, S.-I. Chou, S. Ramakrishna, S. Peng, Tailoring the structure of silicon-based materials for lithium-ion batteries via electrospinning technology, *eScience* 1 (2021) 141–162.
- [20] E.C. David Balcells, Odile Eisenstein, C-H bond activation in transition metal species from a computational perspective, *Chem. Rev.* 110 (2010) 749–823.
- [21] S.V.T. Punniyamurthy, Javed Iqbal, Recent advances in transition metal catalyzed oxidation of organic substrates with molecular oxygen, *Chem. Rev.* 105 (2005) 2329–2364.
- [22] X. Lang, X. Chen, J. Zhao, Heterogeneous visible light photocatalysis for selective organic transformations, *Chem. Soc. Rev.* 43 (2014) 473–486.
- [23] Q. Fan, G.V. Biesold-McGee, J. Ma, Q. Xu, S. Pan, J. Peng, Z. Lin, Lead-free halide perovskite nanocrystals: crystal structures, synthesis, stabilities, and optical properties, *Angew. Chem. Int. Ed.* 59 (2020) 1030–1046.
- [24] T. Krishnamoorthy, H. Ding, C. Yan, W.L. Leong, T. Baikie, Z. Zhang, M. Sherburne, S. Li, M. Asta, N. Mathews, S.G. Mhaikar, Lead-free germanium iodide perovskite materials for photovoltaic applications, *J. Mater. Chem. A* 3 (2015) 23829–23832.
- [25] N.K. Noel, S.D. Stranks, A. Abate, C. Wehrenfennig, S. Guarnera, A.-A. Haghighirad, A. Sadhanala, G.E. Eperon, S.K. Pathak, M.B. Johnston, A. Petrozza, L.M. Herz, H.J. Snaith, Lead-free organic-inorganic tin halide perovskites for photovoltaic applications, *Energy Environ. Sci.* 7 (2014) 3061–3068.
- [26] S.S. Bhosale, A.K. Kharade, E. Jokar, A. Fathi, S.M. Chang, E.W. Diau, Mechanism of photocatalytic  $\text{CO}_2$  reduction by bismuth-based perovskite nanocrystals at the gas-solid interface, *J. Am. Chem. Soc.* 141 (2019) 20434–20442.
- [27] Z. Cui, P. Wang, Y. Wu, X. Liu, G. Chen, P. Gao, Q. Zhang, Z. Wang, Z. Zheng, H. Cheng, Y. Liu, Y. Dai, B. Huang, Space-confined growth of lead-free halide perovskite  $\text{Cs}_3\text{Bi}_2\text{Br}_9$  in MCM-41 molecular sieve as an efficient photocatalyst for  $\text{CO}_2$  reduction at the gas-solid condition under visible light, *Appl. Catal. B: Environ.* 310 (2022), 121375.
- [28] H. Mai, D. Chen, Y. Tachibana, H. Suzuki, R. Abe, R.A. Caruso, Developing sustainable, high-performance perovskites in photocatalysis: design strategies and applications, *Chem. Soc. Rev.* 50 (2021) 13692–13729.
- [29] H. Huang, B. Pradhan, J. Hofkens, M.B.J. Roelfaers, J.A. Steele, Solar-driven metal halide perovskite photocatalysis: design, stability, and performance, *ACS Energy Lett.* 5 (2020) 1107–1123.
- [30] S. Bai, J. Jiang, Q. Zhang, Y. Xiong, Steering charge kinetics in photocatalysis: intersection of materials syntheses, characterization techniques and theoretical simulations, *Chem. Soc. Rev.* 44 (2015) 2893–2939.
- [31] Z.H. Xingyu Liu, Haitao Wang, Tuo Wang, Zhurui Shen, Hao Zhang, Sihui Zhan, Jinlong Gong, Enhanced localized dipole of Pt-Au single-site catalyst for solar water splitting, *PNAS* 119 (2022), e2119723119.
- [32] J. Schneider, M. Matsuoka, M. Takeuchi, J. Zhang, Y. Horiuchi, M. Anpo, D. W. Bahnemann, Understanding  $\text{TiO}_2$  photocatalysis: mechanisms and materials, *Chem. Rev.* 114 (2014) 9919–9986.
- [33] H. Lu, W. Tian, B. Gu, Y. Zhu, L. Li,  $\text{TiO}_2$  electron transport bilayer for highly efficient planar perovskite solar cell, *Small* 13 (2017) 1701535.
- [34] C. Hou, Q. Zhang, Y. Li, H. Wang, P25-graphene hydrogels: room-temperature synthesis and application for removal of methylene blue from aqueous solution, *J. Hazard. Mater.* 205–206 (2012) 229–235.
- [35] J. Li, X. Li, S. Yu, S. Gao, Y. Zhang, Y. Li, C. Wang, Q. Wang, Photocatalytic fuel cell for simultaneous antibiotic wastewater treatment and electricity production by anatase  $\text{TiO}_2$  nanoparticles anchored on Ni foam, *Chin. Chem. Lett.* 34 (2023), 107417.
- [36] X.L. Hao Zhang, Yueming Li, Ying Wang, Jinghong Li, P25-graphene composite as a high performance photocatalyst, *ACS Nano* 4 (2009) 380–386.
- [37] P. Cheng, K. Han, J. Chen, Recent advances in lead-free halide perovskites for photocatalysis, *ACS Mater. Lett.* (2022) 60–78.
- [38] A.D. Taylor, Q. Sun, K.P. Goetz, Q. An, T. Schramm, Y. Hofstetter, M. Litterst, F. Paulus, Y. Vaynzof, A general approach to high-efficiency perovskite solar cells by any antisolvent, *Nat. Commun.* 12 (2021) 1878.
- [39] J. Sun, F. Li, J. Yuan, W. Ma, Advances in metal halide perovskite film preparation: the role of anti-solvent treatment, *Small Methods* 5 (2021) 2100046.
- [40] Y. Yun, F. Wang, H. Huang, Y. Fang, S. Liu, W. Huang, Z. Cheng, Y. Liu, Y. Cao, M. Gao, L. Zhu, L. Wang, T. Qin, W. Huang, A. Nontoxic, Bifunctional anti solvent as digestive-ripening agent for high-performance perovskite solar cells, *Adv. Mater.* 32 (2020) 1907123.
- [41] W. Xu, Y. Gao, W. Ming, F. He, J. Li, X.H. Zhu, F. Kang, J. Li, G. Wei, Suppressing defects-induced nonradiative recombination for efficient perovskite solar cells through green antisolvent engineering, *Adv. Mater.* 32 (2020) 2003965.
- [42] Z. Guan, Y. Wu, P. Wang, Q. Zhang, Z. Wang, Z. Zheng, Y. Liu, Y. Dai, M.-H. Whangbo, B. Huang, Perovskite photocatalyst  $\text{CsPbBr}_{3-x}\text{I}_x$  with a bandgap funnel structure for  $\text{H}_2$  evolution under visible light, *Appl. Catal. B: Environ.* 245 (2019) 522–527.
- [43] Q. Li, T. Song, Y. Zhang, Q. Wang, Y. Yang, Boosting photocatalytic activity and stability of lead-free  $\text{Cs}_3\text{Bi}_2\text{Br}_9$  perovskite nanocrystals via in situ growth on monolayer 2D  $\text{Ti}_3\text{C}_2\text{T}_x$  MXene for C-H bond oxidation, *ACS Appl. Mater. Interfaces* 13 (2021) 27323–27333.
- [44] L. Liu, Y. Jiang, H. Zhao, J. Chen, J. Cheng, K. Yang, Y. Li, Engineering coexposed {001} and {101} facets in oxygen-deficient  $\text{TiO}_2$  nanocrystals for enhanced  $\text{CO}_2$  photoreduction under visible light, *ACS Catal.* 6 (2016) 1097–1108.
- [45] M. Shi, G. Li, W. Tian, S. Jin, X. Tao, Y. Jiang, E.A. Pidko, R. Li, C. Li, Understanding the effect of crystalline structural transformation for lead-free inorganic halide perovskites, *Adv. Mater.* 32 (2020), e2002137.
- [46] L. Wang, B. Cheng, L. Zhang, J. Yu, In situ irradiated XPS investigation on S-scheme  $\text{TiO}_2/\text{ZnIn}_2\text{S}_4$  photocatalyst for efficient photocatalytic  $\text{CO}_2$  reduction, *Small* 17 (2021), e2103447.
- [47] S.N. Andrew, M. Smith, Semiconductor nanocrystals: structure, properties, and band gap engineering, *Acc. Chem. Res.* 43 (2010) 190–200.
- [48] D. Dolat, N. Quici, E. Kusiak-Nejman, A.W. Morawski, G. Li Puma, One-step, hydrothermal synthesis of nitrogen, carbon co-doped titanium dioxide ( $\text{N,C-TiO}_2$ ) photocatalysts. Effect of alcohol degree and chain length as carbon dopant precursors on photocatalytic activity and catalyst deactivation, *Appl. Catal. B: Environ.* 115–116 (2012) 81–89.
- [49] D. Wang, M.A. Mueses, J.A.C. Marquez, F. Machuca-Martinez, I. Grcic, R. Peralta Muniz Moreira, G. Li Puma, Engineering and modeling perspectives on photocatalytic reactors for water treatment, *Water Res.* 202 (2021), 117421.
- [50] R. Acosta-Herazo, M.A. Mueses, G.L. Puma, F. Machuca-Martinez, Impact of photocatalyst optical properties on the efficiency of solar photocatalytic reactors rationalized by the concepts of initial rate of photon absorption (IRPA) dimensionless boundary layer of photon absorption and apparent optical thickness, *Chem. Eng. J.* 356 (2019) 839–849.
- [51] I. Grcić, G. Li Puma, Six-flux absorption-scattering models for photocatalysis under wide-spectrum irradiation sources in annular and flat reactors using catalysts with different optical properties, *Appl. Catal. B: Environ.* 211 (2017) 222–234.
- [52] G. Li Puma, V. Puddu, H.K. Tsang, A. Gora, B. Toepfer, Photocatalytic oxidation of multicomponent mixtures of estrogens (estrone (E1), 17 $\beta$ -estradiol (E2), 17 $\alpha$ -ethynylestradiol (EE2) and estril (E3)) under UVA and UVC radiation: photon absorption, quantum yields and rate constants independent of photon absorption, *Appl. Catal. B: Environ.* 99 (2010) 388–397.
- [53] Z. Li, B. Gao, G.Z. Chen, R. Mokaya, S. Sotiropoulos, G. Li Puma, Carbon nanotube/titanium dioxide (CNT/ $\text{TiO}_2$ ) core-shell nanocomposites with tailored shell thickness, CNT content and photocatalytic/photoelectrocatalytic properties, *Appl. Catal. B: Environ.* 110 (2011) 50–57.
- [54] I. Grcic, G. Li Puma, Photocatalytic degradation of water contaminants in multiple photoreactors and evaluation of reaction kinetic constants independent of photon absorption, irradiance, reactor geometry, and hydrodynamics, *Environ. Sci. Technol.* 47 (2013) 13702–13711.
- [55] D. Dai, X. Liang, B. Zhang, Y. Wang, Q. Wu, X. Bao, Z. Wang, Z. Zheng, H. Cheng, Y. Dai, B. Huang, P. Wang, Strain adjustment realizes the photocatalytic overall water splitting on tetragonal Zircon  $\text{BiVO}_4$ , *Adv. Sci.* 9 (2022), e2105299.

- [56] H. Zhang, C. Cheng, Three-dimensional FTO/TiO<sub>2</sub>/BiVO<sub>4</sub> composite inverse opals photoanode with excellent photoelectrochemical performance, *ACS Energy Lett.* 2 (2017) 813–821.
- [57] H. Huang, H. Yuan, K.P.F. Janssen, G. Solís-Fernández, Y. Wang, C.Y.X. Tan, D. Jonckheere, E. Debroye, J. Long, J. Hendrix, J. Hofkens, J.A. Steele, M.B. J. Roefsaers, Efficient and selective photocatalytic oxidation of benzylic alcohols with hybrid organic–inorganic perovskite materials, *ACS Energy Lett.* 3 (2018) 755–759.
- [58] Z. Zhang, M. Wang, Z. Chi, W. Li, H. Yu, N. Yang, H. Yu, Internal electric field engineering step-scheme-based heterojunction using lead-free Cs<sub>3</sub>Bi<sub>2</sub>Br<sub>9</sub> perovskite-modified In<sub>4</sub>SnS<sub>8</sub> for selective photocatalytic CO<sub>2</sub> reduction to CO, *Appl. Catal. B: Environ.* 313 (2022), 121426.
- [59] Z. Jia, X. Wang, F. Thevenet, A. Rousseau, Dynamic probing of plasma-catalytic surface processes: oxidation of toluene on CeO<sub>2</sub>, *Plasma Process. Polym.* 14 (2017) 1600114.
- [60] Z. Zhou, Y.-N. Xie, W. Zhu, H. Zhao, N. Yang, G. Zhao, Selective photoelectrocatalytic tuning of benzyl alcohol to benzaldehyde for enhanced hydrogen production, *Appl. Catal. B: Environ.* 286 (2021), 119868.
- [61] N. Soszka, B. Hachula, M. Tarnacka, E. Kamińska, J. Grelska, K. Jurkiewicz, M. Geppert-Rybczyńska, R. Wrzalik, K. Grzybowska, S. Pawlus, M. Paluch, K. Kamiński, The impact of the length of alkyl chain on the behavior of benzyl alcohol homologues—the interplay between dispersive and hydrogen bond interactions, *Phys. Chem. Chem. Phys.* 23 (2021) 23796–23807.
- [62] Y.L. Geir, M. Førland, et al., Associative behavior of benzyl alcohol in carbon tetrachloride, *Solut., J. Phys. Chem. B* 101 (1997) 6960–6969.
- [63] N.-Mn RafaelMéndez-Román, Relationship between the formation of surface species and catalyst deactivation during the gas-phase photocatalytic oxidation of toluene, *Catal. Today* 40 (1998) 353–365.
- [64] D.F. Csilla Keresszegi, Tamas Mallat, et al., Unraveling the surface reactions during liquid-phase oxidation of benzyl alcohol on Pd/Al<sub>2</sub>O<sub>3</sub>: an in situ ATR–IR study, *J. Phys. Chem. B* 109 (2005) 958–967.
- [65] H. Huang, J. Zhao, Y. Du, C. Zhou, M. Zhang, Z. Wang, Y. Weng, J. Long, J. Hofkens, J.A. Steele, M.B.J. Roefsaers, Direct Z-scheme heterojunction of semicoherent FAPbBr<sub>3</sub>/Bi<sub>2</sub>WO<sub>6</sub> interface for photoredox reaction with large driving force, *ACS Nano* 14 (2020) 16689–16697.